RAA 2020 Vol. **20** No. **1**, 12(14pp) doi: 10.1088/1674–4527/20/1/12

http://www.raa-journal.org *http://iopscience.iop.org/raa*

Research in Astronomy and Astrophysics

Development of image motion compensation system for 1.3 m telescope at Vainu Bappu Observatory

Sreekanth Reddy Vallapureddy⋆, Ravinder Kumar Banyal, Sridharan Rengaswamy, P Umesh Kamath and Aishwarya Selvaraj

Indian Institute of Astrophysics, Bangalore 560034, India; *sreekanth@iiap.res.in*

Received 2019 July 16; accepted 2019 August 28

Abstract We developed a tip-tilt system to compensate the turbulence induced image motion for the 1.3 m telescope at Vainu Bappu Observatory, at Kavalur. The instrument is designed to operate at the visible wavelength band $(480-700\,\mathrm{nm})$ with a field of view of $1' \times 1'$. The tilt corrected images have demonstrated up to $\approx 57\%$ improvement in image resolution and a corresponding peak intensity increase by a factor of ≈ 2.8. A closed-loop correction bandwidth of $\approx 26\,\mathrm{Hz}$ has been achieved with on-sky tests and the root mean square motion of the star image has been reduced by a factor of ~ 14. These results are consistent with theoretical and numerical predictions of wave-front aberrations caused by atmospheric turbulence and image quality improvement expected from a real-time control system. In this paper, we present details of the instrument design, laboratory calibration studies and quantify its performance on the telescope.

Key words: adaptive optics — atmospheric effects — high angular resolution

1 INTRODUCTION

Soon after the telescope was developed, it was realized that atmospheric turbulence poses a major hindrance to the performance of ground-based telescopes. The effects of atmospheric turbulence on astronomical observations were investigated by Fried (1965, 1966a) by relating the statistics of wave distortion to optical resolution. Extensive research on the effect of atmospheric studies indicated that imaging through turbulence is limited by atmospheric seeing λ/r_0, irrespective of optical system resolution λ/D, where r_0 is the Fried parameter and D is the aperture diameter.

The turbulence induced wave-front distortions are often spread over different spatial scales. The study by Noll (1976) expressed these distortions using Zernike polynomials representing varying degrees of aberration. These polynomials are widely applied to evaluate optical system performance. The same approach was employed by Noll (1976) to estimate the effect of atmospheric turbulence on a wave-front. From these investigations, it became clear that the effect of wave-front distortions scales with the size of the system aperture, with a larger telescope leading to stronger deleterious effects on higher-order distortions. The image motion, being the lowest order aberration, is primarily caused by the global tilt in the wave-front, sometimes also called the angle of arrival fluctuations. The contribution of the lowest order distortions is about 87% of the wave-front phase variance (Fried 1965; Dainty et al. 1998). By eliminating the image motion using a real-time tip-tilt system, the image resolution can be significantly improved, at least for small aperture diameters.

Optical wave-front correction with an adaptive optics (AO) system was first used by the US Navy for defence purposes (Greenwood 1977). Its enormous potential was also recognized in the fields of medical and astronomical applications. One of the early realizations of astronomical AO systems, the COME-ON prototype system, was on Observatoire de Haute-Provence (Rousset et al. 1990). Modern telescopes equipped with AO are highly productive and serve the astronomical community better.

The design and development of an AO system should consider the atmospheric characteristics of the telescopic site. Apart from telescope size, the Fried parameter (Fried 1966b), isoplanatic angle (Hubbard et al. 1979) and coherence time (Davis & Tango 1996; Kellerer & Tokovinin 2007) are the key parameters that can guide the design of an AO system. The Fried parameter determines the minimum spatial sampling of the wave-front for sensing and correction. The coherence time helps to determine the optimal loop frequency for closed-loop AO operation. For high-speed operation, the target star should have enough

⋆ Corresponding author

photons to adequately sample the wave-front, both temporally and spatially. This limits the operation of natural guide star AO systems to a small number of target stars that are relatively brighter (Wizinowich et al. 2000). Therefore, to increase the overall sky coverage and improve the effective AO correction over a large angular range, single or multiple artificial laser guide stars are often deployed (Max et al. 1997).

The knowledge of isoplanatic angle is essential in natural guide star systems. In the case of fainter science targets, the AO system relies on a nearby bright target as a guide star, preferably within an isoplanatic angle. The proximity of the science target to the guide star defines the active correction of the wave-front. Typically, this parameter will range from $2'' - 6''$ (Eaton et al. 1985; Sarazin & Tokovinin 2002).

Conventionally, AO systems initially correct the slope (global tilt with large amplitude) of the wave-front before they correct high-order distortions (high spatial frequency terms with smaller amplitudes). In the former case, a rapidly moving two-axis steering mirror is used for correcting variations in the wave-front slope. Such a system is conceptually simple to develop and cost effective. The layout of a natural guide star tip-tilt correction system is illustrated in Figure 1. This system has a tip-tilt stage with a mirror mounted on it. In response to changing conditions, the tip-tilt controller constantly steers the actuators to keep the stellar beam locked to a fixed reference position in the image plane. A number of tip-tilt systems have been developed in the past (Racine & McClure 1989; Glindemann et al. 1997). A tip-tilt system at the Calar Alto 3.5 m telescope, for example, has demonstrated reduction in image motion from $\sim \pm 0.4''$ to $\sim 0.03''$ with $30-100$ Hz loop frequency (Glindemann et al. 1997). This alone could yield a significant improvement in image resolution. Proper exposure time for a tip-tilt sensor is crucial to optimize the performance of the instrument (Martin 1987). For example, Glindemann (1997) has demonstrated that to track/correct image motion with a $5-10$ Hz bandwidth, a loop frequency of $50-100$ Hz is required. Close & McCarthy (1994) developed a Cassegrain secondary tip-tilt AO. They reported three-fold image motion reduction at a loop frequency of 72 Hz. Furthermore, Golimowski et al. (1992) implemented an image motion compensation system for high resolution stellar coronography. The instrument is reported to have achieved a resolution gain by a factor of 2.2. It enabled the observations of two magnitude fainter objects than what was achieved without the image stabilization.

The Indian Institute of Astrophysics has initiated a long-term project to develop AO systems for its observatory telescopes. We plan to achieve this in three phases: first, estimating the turbulence parameters at the telescope site, second, the development of a tip-tilt image motion compensation system and third, the design and implementation of a higher order AO system. Atmospheric turbulence parameters, namely, the Fried parameter, isokinetic angle and coherence time have been measured in the initial phase (Sreekanth et al. 2019). In this paper, we discuss the design and development of a tip-tilt system for the 1.3 m telescope at Vainu Bappu Observatory (VBO), at Kavalur. From here on, the paper is organized as follows. In Section 2 we present the details of opto-mechanical design of the instrument followed by the development of control software and tip-tilt calibration methodology. Laboratory tests and characterization of the instrument are discussed in Section 3. The on-sky performance of the instrument is described in Section 4. Finally, in Section 5, we summarize our results.

2 OPTO-MECHANICAL DESIGN

The tip-tilt system was designed for the 1.3 m telescope at VBO, located at $78°50'$E and $12°34'$N. The telescope was commissioned in 2014. It is a Ritchey-Chretién model telescope with the primary and secondary being hyperbolic mirrors. During routine observations, the telescope resolution is seeing-limited. A tip-tilt instrument followed by a higher order AO system is envisioned to transform the seeing-limited resolution of the telescope to the near diffraction limited case.

2.1 Opto-mechanical Design

The optical system of the instrument was designed in ZEMAX ray tracing software. Several design parameters, such as effective focal length, overall weight and dimensions of the instrument, were considered. The pixel scale at the telescope's Cassegrain focus is $0.26''$ pixel^{-1} (pixel size $= 13\,\mu$m) while the diffraction limited resolution is $0.106''$ at a wavelength of 630 nm. In the optical design of the instrument, the pixel scale was reduced to half of the diffraction limited resolution. This improved the sensitivity of the telescope to measure the image motion. The instrument weighs ≈ 28 kg and has dimensions $120 \times 60 \times 30\,\mathrm{cm}^3$. It was installed on the West port of the telescope as depicted in the top panel of Figure 2. A solid model designed in $AutoCAD$ is shown in the bottom panel of Figure 2. Some key specifications of the telescope and the tip-tilt instrument are listed in Table 1.

2.2 Sub-components of the Instrument

A brief description of essential sub-components of the tip-tilt instrument is as follows.

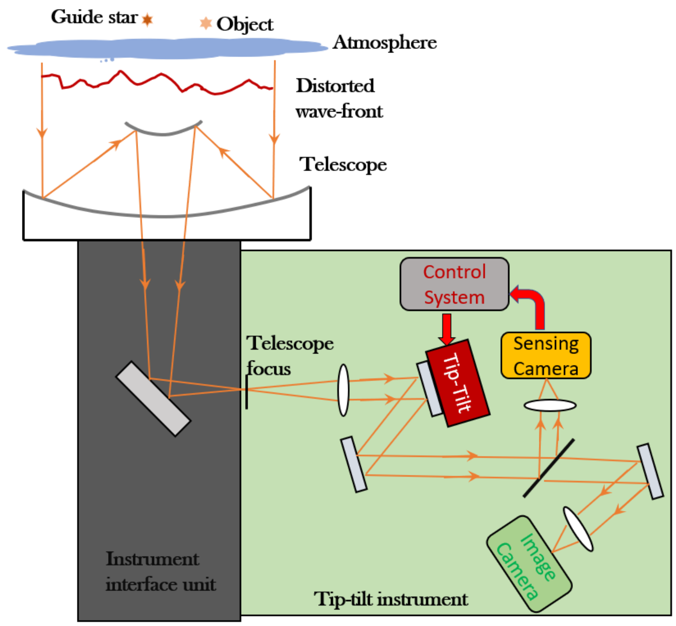

Fig. 1 Conceptual layout of a natural guide star tip-tilt correction system. The telescope primary mirror collects light from a target field. The light beam is directed to the tip-tilt instrument, then the light is divided between the sensing arm and the imaging arm of the instrument. The image motion is corrected in a common path where the tip-tilt stage is placed. The corrected wave-front can be directed to an imaging camera or science instrument.

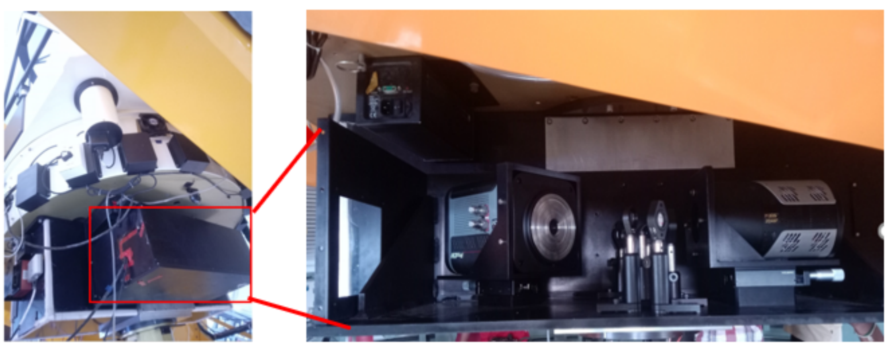

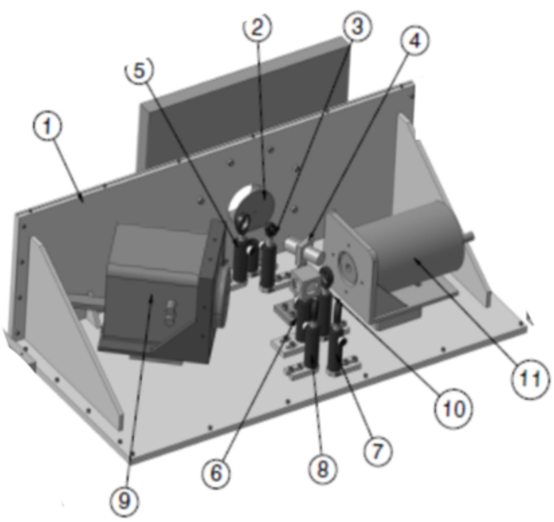

S.N.	ITEM	QTY.
1	BASE	1
2	FIELD STOP ASSEMBLY	1
3	LENSE L1 ASSEMBLY	1
4	TIP TILT STAGE ASSEMBLY	1
5	FOLD MIRROR ASSEMBLY	1
6	BEAM SPLITTER ASSEMBLY	1
7	FOLD MIRROR-2	1
8	LENSE L2 ASSEMBLEY	1
9	IMAGE CAMERA ASSEMBLY	1
10	LENSE L3 ASSEMBLY	1
11	SENSE CAMERA ASSEMBLY	1

Fig. 2 The tip-tilt instrument mounted on the West port of the Cassegrain focus of the 1.3 m JCB telescope at VBO (*top*). A CAD model showing the mechanical layout and system components (*bottom*).

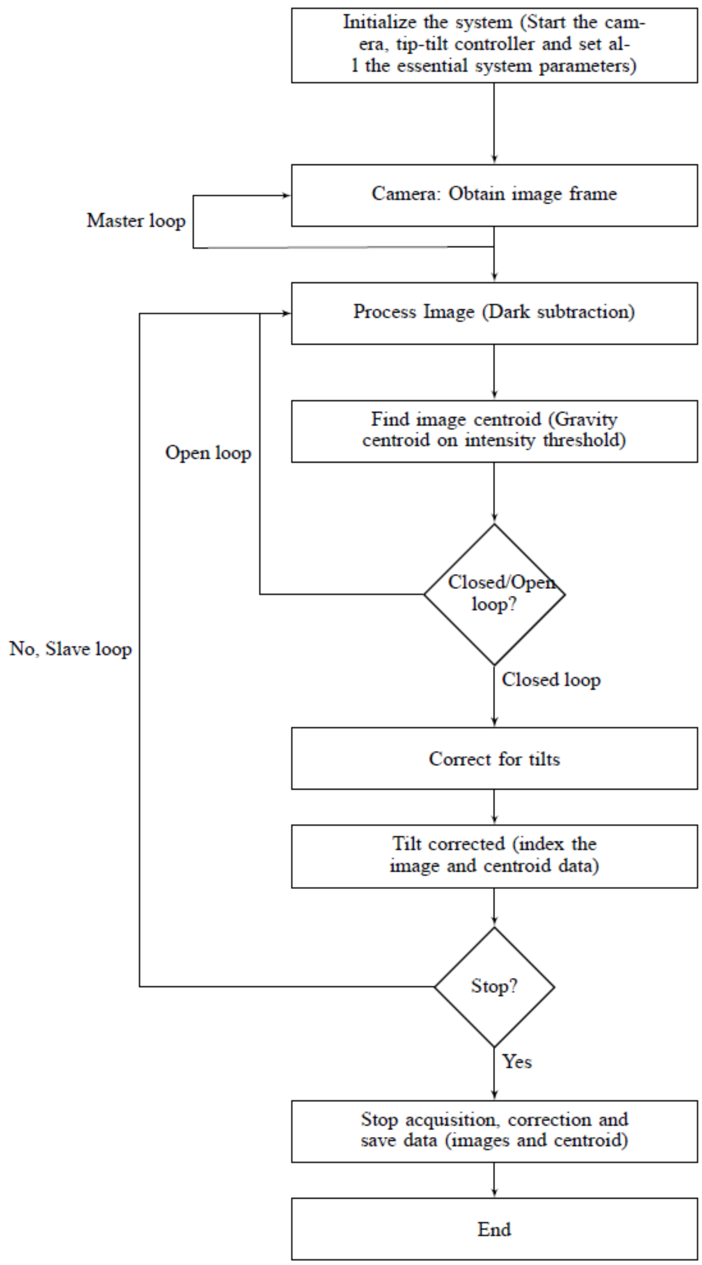

Fig. 3 Flow chart for control software.

Table 1 Key specifications of the tip-tilt instrument. Telescope and instrument layout are displayed in Fig. 1. $F/_{\#}$: F-ratio, PS: Pixel Scale.

Property	Value
Wavelength range	$480 - 700\,\mathrm{nm}$
wave-front sensing plane FOV2	$40''$
Image plane FOV1	$1'$
Telescope focus $F/_{\#}$, PS	$8, 0.26''$
Sensor camera $F/_{\#}$, PS	$15.7, 0.06''$
Imaging camera $F/_{\#}$, PS	$22.4, 0.08''$

- **Tip-tilt stage**: We used a fast steering tip-tilt stage from *Physik Instrumente*[1] (Model: S-330). It is a piezo-based actuator system with two orthogonal axes. Each of the axes has two actuators that work on the opposite polarity of an applied voltage. These axes are able to deflect the light beam with 0.5 μrad resolution over a 10 mrad tilt angle. The tip-tilt stage has a one-inch diameter platform to mount a mirror that steers the light beam projected on to it. The stage is driven by a *Physik Instrumente* E-517 control system that has

[1] `https://www.physikinstrumente.com/`

proportional, integral and differential (PID) internal voltage controller to provide a positional accuracy of 0.5 μrad in closed-loop operation.

- **Sensing camera**: The performance of the tip-tilt instrument depends on its ability to sense the image motion and apply the necessary correction. The sensing camera should be able to operate at high frame rate to record random drift in the stellar image. We installed an *Andor Neo-sCMOS* 2560×2160 pixel high-speed camera[2]. For exposure time of 1 ms and frame size of 128×128 pixels, we were able to achieve a frame rate of ~ 300 using control software developed on the LabView platform. With a 6.5 μm pixel size and magnification achieved by the relay optics, the sensing camera is able to sample the sky with resolution of $0.06''$ pixel^{-1}.
- **Imaging camera**: We implemented a *Princeton Instruments* ProEm eXcelon (1024×1024, pixel size $=$ 13μm) EMCCD[3] for tilt corrected observations. The CCD is run in continuous exposure mode with simultaneous read out of the data. This is a frame transfer operation. In this mode, data in the active area are vertically shifted to a masked area. This operation takes around a microsecond (0.8 μsec) and enables the active area to be available for the next exposure. The full frame of the CCD covers $\approx 1' \times 1'$ on-sky field of view (FoV) with plate scale of $0.08''$pixel^{-1}.

2.3 Estimation of Image Motion

The sensing camera is operated in high-speed mode (~ 300 fps) to acquire short exposure images. These images were used to estimate the image motion by applying a centroid tracking method (Close & McCarthy 1994; Golimowski et al. 1992). Noise in the images affects the accuracy of centroid tracking. The images were bias subtracted. Although the magnitude of the dark current itself is negligible, there is considerable bias counts (~ 100 counts at 30 K), which contributes error to the centroid estimation. Thus, this 'dark' subtraction (which includes bias) was found to be essential. The master dark is obtained by taking the median of the dark frames before each experiment.

The centroid estimation should be faster to minimize the time delay between sensing of the motion and the correction. For this experiment, we have chosen an intensity thresholding centroid technique. In this method, a threshold slightly above the pixel noise level is applied to the image. The method minimizes the noise by assigning zero counts to pixels below the threshold. The resultant image centroid is measured using the weighted average of the intensities as expressed in Equation (1). To measure the improvement in tilt corrected image motion, the root mean square (rms) of the residual centroid motion is estimated via Equation (2)

$$X_c = \frac{\sum x_i I_i}{\sum I_i}, Y_c = \frac{\sum y_i I_i}{\sum I_i}, \tag{1}$$

$$\sigma_x = \sqrt{\frac{\sum (X_c - \bar{X}_c)^2}{n}}, \sigma_y = \sqrt{\frac{\sum (Y_c - \bar{Y}_c)^2}{n}}, \tag{2}$$

where X_c, Y_c are the estimated centroid of the image, $I_{i,j}$ is pixel intensities, $x_{i,j}$, $y_{i,j}$ are pixel coordinates, $\bar{X}_c$, $\bar{Y}_c$ are mean centroids and σ_x, σ_y are associated standard deviations.

2.4 Power Spectral Density

The power spectral density (PSD) is the measure of energy distributed over a frequency range when the measurements are made within a finite time window (Welch 1967). In this paper, the PSD of the centroids of tilt uncorrected and corrected images was measured. Comparisons between the PSDs help in determining the correction bandwidth of the tip-tilt instrument. The correction bandwidth is defined as the lowest frequency at which the ratio of the PSD of the uncorrected and corrected data sets falls to unity, i.e., dB.

$$\widehat{x}(f) = \frac{1}{2\pi\sqrt{T}} \int_0^T e^{-2\pi i f t} x(t) dt, \tag{3}$$

$$S(f) = |\widehat{x}(f)|^2. \tag{4}$$

The PSD $S(f)$ generated over limited time interval $[0, T]$ of centroid data $x(t)$ is defined in Equations (3) and (4). Whereas, $\widehat{x}(f)$ is the Fourier transform of centroid data with temporal frequency f.

2.5 Control Software

Control software with a graphical user interface (GUI) was developed using National Instrument's LabVIEW platform[4] to operate the instrument. The software enables interoperability between the sensing camera and the tip-tilt stage. The program flow of the control software is displayed in the Figure 3. As illustrated in the flowchart, during the initialization step, the connectivity of the tip-tilt stage and the camera is checked. Subsequently, the exposure time and number of frames to obtain are set, following which the tip-tilt actuators are initialized. The program has one master loop and one slave loop where the former independently acquires image frames, and the later processes

[2] `https://andor.oxinst.com`
[3] `https://www.princetoninstruments.com/`
[4] `http://www.ni.com/`

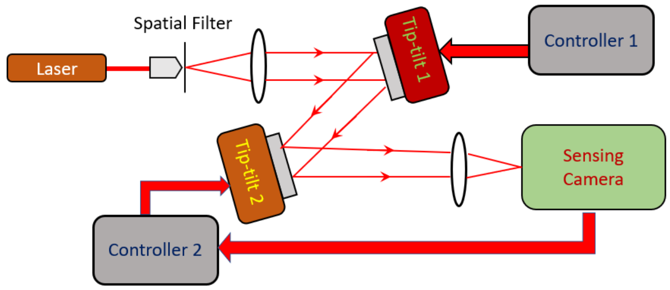

Fig. 4 Experimental layout for the tip-tilt calibration in the lab. The tip-tilt stage TT1 is utilized to induce the image motion while TT2 is operated to correct it. The CCD camera records movement of the laser spot.

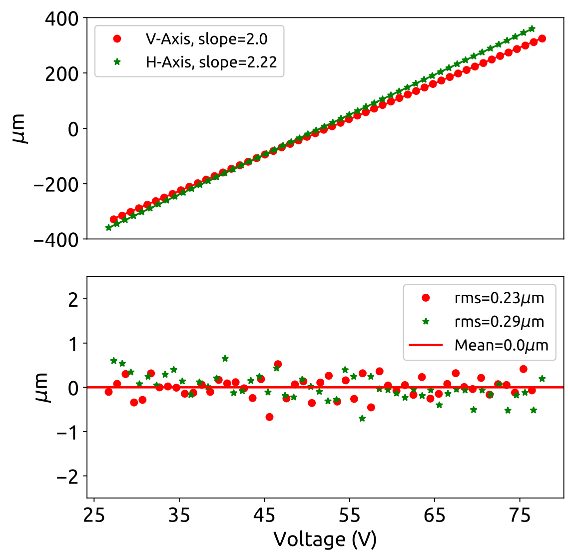

Fig. 5 Calibration curves for two-axis tip-tilt stage. The horizontal (H-axis) and vertical (V-axis) axes have been moved with equal step size of 1 V (*top*). In both cases, the rms deviation from the linear fit is ~ 0.3 µm (*bottom*).

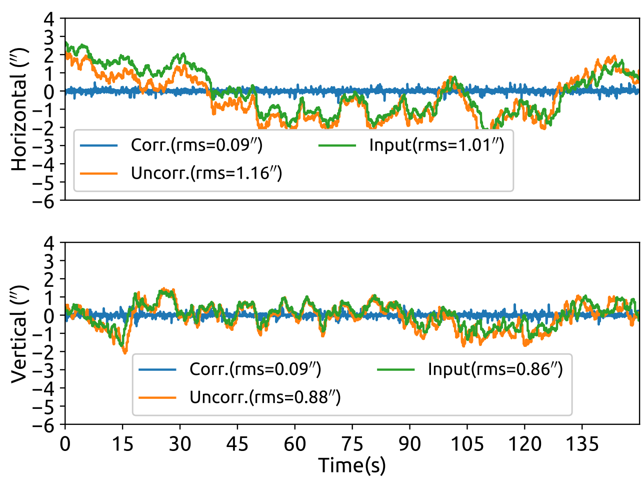

Fig. 6 Image centroid motion in arcsec (″) along horizontal (*top panel*) and vertical (*bottom panel*) axes of the camera. The plot has three sets of data, i.e., the induced image motion, the uncorrected image motion and the corrected residual image motion. The induced and sensed image motions have $\sim 96\%$ correlation. The image shift is converted to arcsec by multiplying the image shift by pixel scale, and is similar to that of the telescope (0.06″).

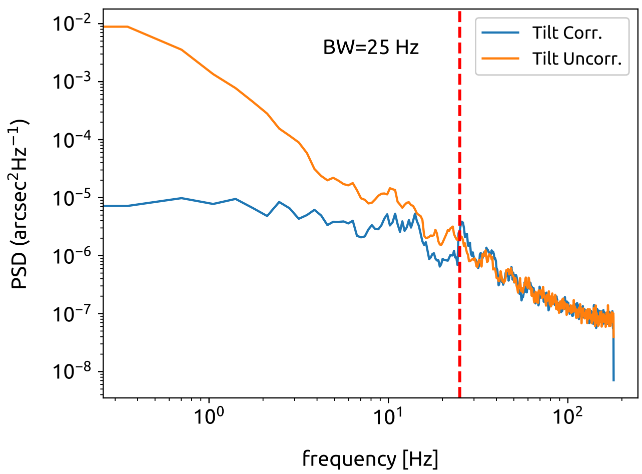

Fig. 7 The PSD of centroid data in the laboratory. The *vertical line* signifies merging of the two plots. This is the 0 dB closed-loop correction bandwidth (*red line*) of the system.

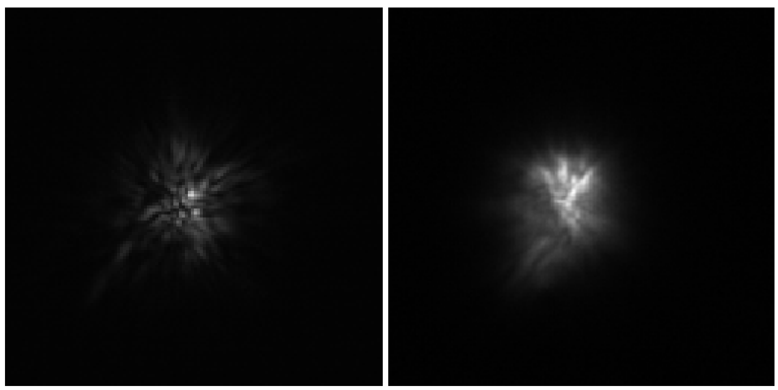

Fig. 8 Illustration object: HIP57632. The short exposure time (3 ms) image on sensing camera (*left*). Relatively long exposure time (200 ms) image on the imaging camera. The frame size is $\sim 10'' \times 10''$.

them in sequence to estimate the centroid. The independence of the master loop from its slave improves the loop frequency of the system. The tip-tilt stage corrects for each of the centroid shifts in real time to compensate for image motion. There is a time delay of ≈ 0.8 ms, after acquiring the image and the tip-tilt mirror reaching its commanded position. The software features an option to save the image and centroid data. For optimal performance of the instrument in closed loop, a PID controller was implemented in the software.

$$\Delta c(t) = K_p e(t) + K_d \frac{de(t)}{dt} + K_i \int_0^{t'} e(t')dt \,. \qquad (5)$$

In the above equation, K_p, K_d and K_i are proportional, derivative and integral gains, respectively, $e(t)$ is the difference between two consecutive centroid shifts, and $\Delta c(t)$ is the centroid shift estimated using the PID control. The controller gains are calculated using the trial and error method by monitoring the residual image centroid motion. The estimated values for K_p, K'_d and K'_i are 4×10^{-1}, 2.5×10^{-1} and 2.3×10^{-3} respectively. Here, K'_d and K'_i are $K_d * T$ and K_i/T respectively, where T is the time interval between two consecutive centroids. The $\Delta c(t)$ is multiplied by voltage required to cause a pixel shift.

2.6 Instrument Calibration

Calibration is required to accurately map the image wandering on the CCD to the input control voltage that drives the piezo actuators to compensate for image movement across the detector plane. This mapping is unique for each instrument as the linear beam-throw by steering mirror depends on the specific layout of the optical components.

The axis of the stage has been centered around its maximum dynamic range, i.e., at five mrad. Layout of the laboratory setup is illustrated in Figure 4. A point source is generated by spatially filtering the laser beam as demonstrated in the figure. The spatial filter consists of a microscope ob-

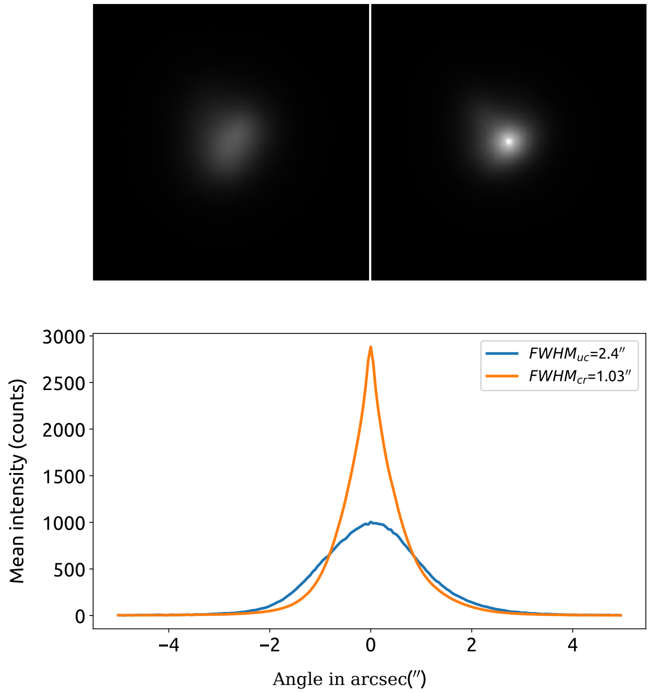

Fig. 9 Illustration: Object HIP57632. The tilt uncorrected (*top-left*) and the tilt corrected (*top-right*) co-added images. The psf of the image along the horizontal axis is shown in the *bottom* panel.

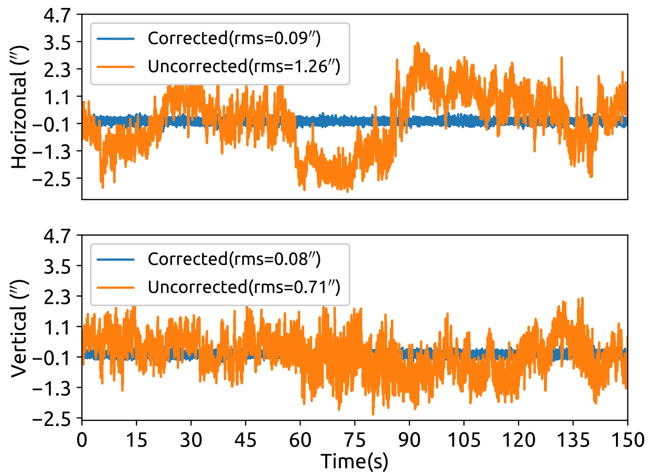

Fig. 10 Image centroid motion of HIP57632. The rms image motion has been reduced by a factor of ~ 14 along the horizontal axis and ~ 8.9 along the vertical axis.

jective and a 10 μm pinhole. For performance analysis, the centroid motion of the point source image on the sensing camera has been observed.

2.6.1 Axis alignment

Ideally, the movement of two actuator axes should be perfectly aligned with the pixel rows (horizontal) and columns (vertical) of the CCD. Initially, the axes of the tip-tilt stage were coarsely aligned by observing the spot traces in the live camera images. After making fine adjustments, a residual deviation in alignment was measured by taking multiple images of the source on the CCD while the beam was progressively steered (horizontally or vertically) in a sequence of voltage steps applied to individual actuators, one at a time. Furthermore, to minimize the alignment error, a rotation matrix (Russell 1971) as expressed in Equation (6) was generated from the obtained data. To compensate the

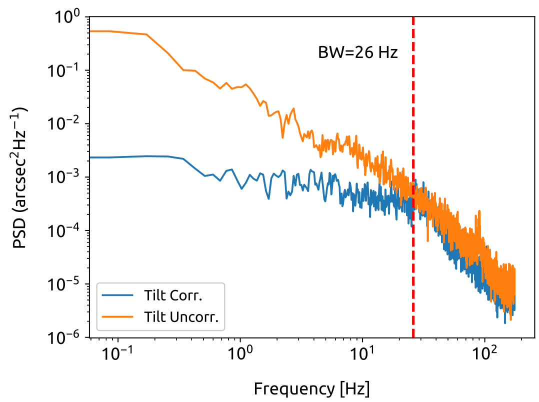

Fig. 11 The PSD of the image motion for star HIP57632. *Vertical dotted line* demarcates the closed-loop bandwidth of the system.

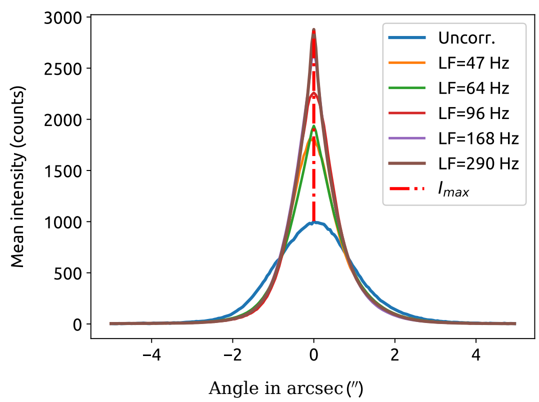

Fig. 12 Comparison of tip-tilt corrected psf of HIP57632 for different loop frequencies. The peak intensity manifests logistic growth with loop frequency.

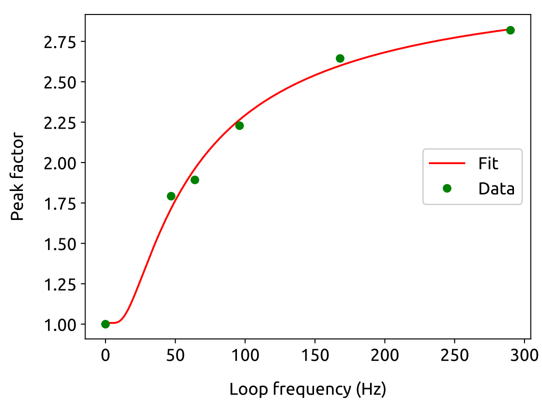

Fig. 13 Increment in peak factor with loop frequency.

small offset in the alignment, the shift in image motion is multiplied by this matrix before applying the corrections in real time.

$$\begin{bmatrix} x' \\ y' \end{bmatrix} = \begin{bmatrix} a & b \\ c & d \end{bmatrix} * \begin{bmatrix} x \\ y \end{bmatrix} . \tag{6}$$

$$X' = AX . \tag{7}$$

$$V = KX' . \tag{8}$$

Equation (7) is the relation between the rotation matrix A and the centroid shifts. In Equation (6), x and y are image centroid shift, and x' and y' are centroid shift after rotation along the H-axis and V-axis respectively. In our experiment, the measured elements of the rotation ma-

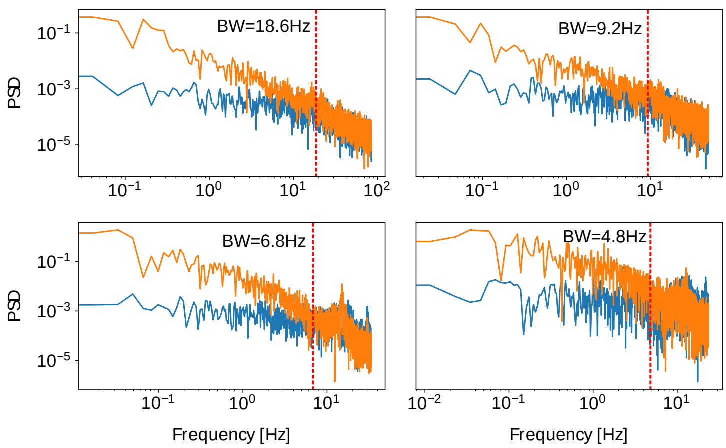

Fig. 14 The PSD (arcsec^2 Hz^{-1}) with respect to correction bandwidth for object HIP57632. The *orange* and *blue lines* are PSD of tilt uncorrected and corrected centroid data respectively. The loop frequency is 168 Hz (*left*) and 96 Hz (*right*) for top row, 64 Hz (*left*) and 47 Hz (*right*) for bottom row, and their correction bandwidths (*red line*) are in the plot.

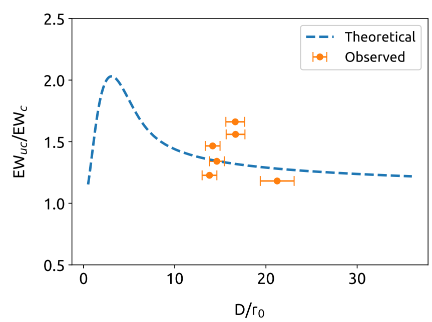

Fig. 15 Comparison of gain in angular resolution between the theoretical and observed data. On the vertical axis, EW$_{uc}$ and EW$_c$ are equivalent widths of tilt uncorrected and corrected images respectively.

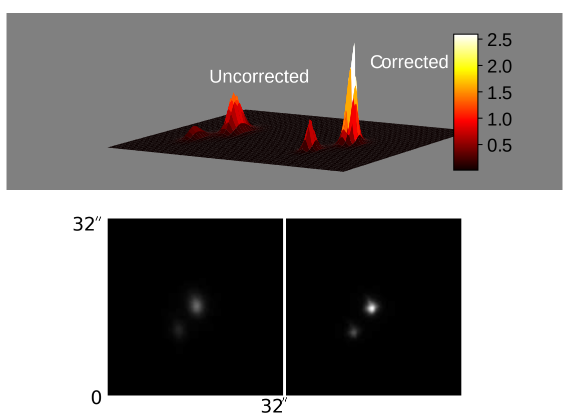

Fig. 16 Surface plot of HIP50583, containing average tilt uncorrected and corrected image. The frame size is $\sim 32'' \times 32''$.

trix (A) were: $a = 1.003$, $b = 0.0013$, $c = 0.0015$ and $d = 0.9996$. These are typical values for a closely aligned system. In Equation (8), V is voltage applied to the tip-tilt stage and K is the voltage per unit shift in the centroid.

The response of each actuator is tested independently by tilting it over a range of 3 mrad to 8 mrad with an input voltage step size of 1 V. The image centroids for each input step voltage are recorded. The mean centroid shift is estimated by measuring the average difference between two

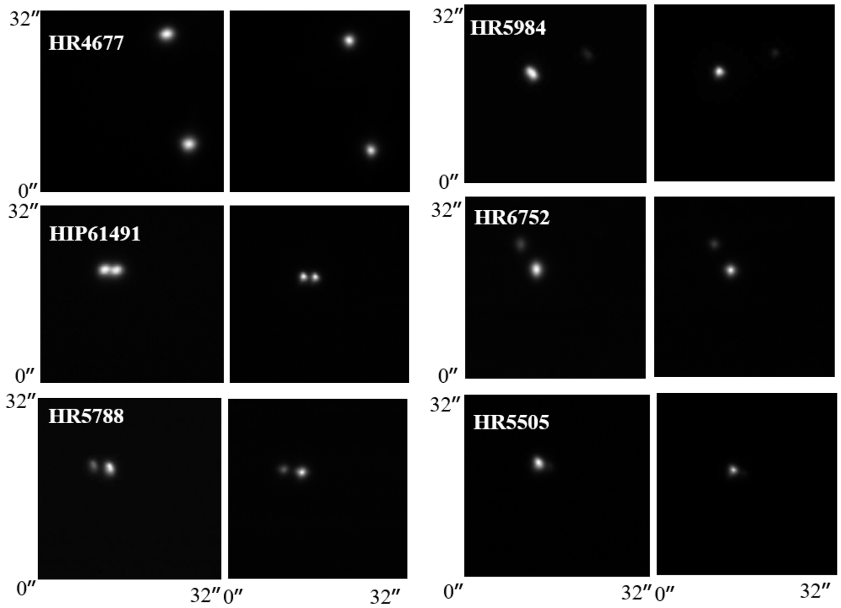

Fig. 17 Examples: Tilt uncorrected and corrected images of various targets.

Table 2 Tip-tilt Stage Axis Calibration

Parameter	Value
Number of samples	51
Exposure time per sample	3 ms
Tip-Tilt range	$3-8$ mrad
Voltage range	$24-78$ V
Voltage step size	~ 1 V
Linear image shift (total)	~ 650 µm
Mean centroid shift	~ 12 µm
rms error in movement	~ 0.3 µm

consecutive centroids over the earlier mentioned tilt range. Figure 5 (top panel) shows the image centroid shift on the camera as a function of input voltage. The error in actuator movement is defined as the difference between two consecutive centroids with respect to the mean centroid shift. It is plotted in the Figure 5 (bottom panel). The estimated rms error in the actuator movement is less than 0.3 µm. Results of tip-tilt stage calibration are summarized in Table 2.

3 LABORATORY TESTING OF THE INSTRUMENT

Initially, a prototype of the instrument was set up in the laboratory. Centroid data of short exposure images of the star were obtained a priori from the telescope. These data were then used as input to one of the steering mirrors to simulate image motion in lab studies. For characterization of the instrument, the residual image centroid motion and the PSD of tilt uncorrected and corrected images were analyzed.

The layout of the laboratory setup is displayed in Figure 4. In this study, we utilized two tip-tilt stages, one to induce the image motion (Piezosystem jena[5], Model Number: PSH x/2); and the other to correct it. The former has frequency response up to 3 kHz, 0.02 µrad resolution and ± 4 mrad dynamic range.

The centroid data (in pixels) need to be converted to voltages which will be applied to the tip-tilt stage 1 (TT1). For this purpose, the per-pixel voltage (0.21 V for H-axis and 0.23 V for V-axis) is estimated for the TT1 system from the calibration curves. The voltages were applied to TT1 to induce image motion at the frequency of 33 Hz. This is to maintain at least 10 times correction bandwidth (Hardy 1998) of the system. The induced image motion is tracked using the centroid estimations.

The image motion data were recorded both with and without the tip-tilt correction. Figure 6 shows the image centroid motion in the laboratory. The rms of corrected image motion is reduced by a factor of ~ 12.8 along the horizontal axis and ~ 9.8 along the vertical axis, compared to the uncorrected case.

The closed-loop correction bandwidth of the system was estimated from the power spectral densities of the image motions for both tilt uncorrected and corrected cases. The observed correction bandwidth (0 dB) is ~ 25 Hz as shown in Figure 7.

4 ON-SKY TESTING OF THE INSTRUMENT

After successful alignment and calibration, the instrument was mounted on the telescope (see Fig. 2). Initial tests were done in March 2018. The on-sky performance of the tip-tilt system is described in terms of the residual rms image

[5] `https://www.piezosystem.com/`

motion, correction bandwidth, full width at half maximum (FWHM) and peak intensity of the image. We are presenting these results after satisfactory performance has been achieved since January 2019.

4.1 Observations

The objects with m_v brighter than six have been chosen. These objects were close to the zenith with hour angle of less than one hour. Preferably, targets with more than one object in the field were chosen. This enables the instrument to sense the bright star with high-speed and apply correction to the entire field. The list of the targets used is given in Table 3. These targets were observed on different days from March 2019 to May 2019.

For high speed performance, a region of interest (ROI) has been chosen around the target image on the sensing camera. This enhanced the frame rate and thus increased the overall loop frequency. The exposure times are chosen from 3 ms to 20 ms. The longer exposure time allows us to observe relatively fainter targets. This enables us to vary the loop frequency from ~ 290 fps to 47 fps. Each data set was recorded over 150 sec. Under poor atmospheric conditions, the binning operation was carried out in the program to enhance the signal to noise ratio. This might have reduced the accuracy in centroid estimation, but overall, it improved the correction performance.

The tilt corrected images were acquired on the imaging camera. This camera was given relatively longer exposure time (~ 200 ms). Because of a set of objects with different magnitude, we chose a fixed exposure time to avoid pixel saturation in case of a brighter object. In Figure 8, short exposure images of the sensing camera and imaging camera are displayed.

A total of 1000 images of each target field was acquired on the imaging camera. Every target was observed for tilt uncorrected and corrected images. These images were processed using a Python script. The image frames have been dark subtracted and flat fielded prior to the analysis. The co-added images, as depicted in Figure 9, will give the equivalently long exposure images. Finally, these images were divided by number of obtained frames. This will average the intensity of each frame and minimize the effect of intensity fluctuations on the estimation of performance.

4.2 Image Centroid, PSD and psf Comparison

The instrument was characterized by measuring the residual image motion. Figure 10 shows the tilt-corrected and uncorrected image centroids recorded consecutively by the sensing camera. The rms value was reduced to $\sim 0.08''$ from $\sim 1.26''$.

The image motion PSD is plotted in Figure 11. The correction bandwidth of the system is found to be ~ 26 Hz, depicted with a vertical line in the figure. The temporal frequencies beyond this limit are uncorrected.

On the imaging camera, the point spread function (psf) is expected to be sharper with the tip-tilt instrument in operation. Figure 9 shows the psf of HIP57632. The FWHM of the psf has improved from $2.4''$ to $1.03''$. The improvement in FWHM was calculated as expressed in Equation (9). This is a $\sim 57\%$ improvement.

$$Improvement(\%) = \frac{FWHM_{uc} - FWHM_{cr}}{FWHM_{uc}} \times 100. \tag{9}$$

Here, $FWHM_{uc}$ is for an uncorrected image and $FHWM_{cr}$ is for a corrected image.

In the above case, the peak intensity of tilt corrected psf has increased by a factor of ~ 2.8. This improves the sensitivity of the instrument towards the observation of a fainter object. The sensitivity was estimated by applying Equation (10). This equation relates the magnitude difference of a star with peak intensity of the tilt uncorrected and corrected images. It is observed that the sensitivity is improved by a factor of 1.1 in magnitude.

$$\Delta m_v = -2.512 * \log_{10}\left[\frac{I_c}{I_{uc}}\right], \tag{10}$$

where I_c/I_{uc} is the ratio of peak intensities of tilt corrected and uncorrected images, and Δm_v is the improvement in apparent magnitude. Here, we consider I_c/I_{uc} as $4.3/1.49$.

4.3 Effect of Loop Frequency

The optimal frame rate is essential for effective tilt correction of the images in closed-loop operation. This confirms the fact that the wave-front distortions are caused by spatial and temporal disturbances in the atmosphere. The spatial distortions are corrected by compensating for the shift in the image centroid, but the dynamic nature of the atmosphere induces high frequency image motion. To overcome this effect, the time delay between the instant that the shifts are estimated and the instant that the correction is applied to the corrector should be kept minimum.

To study the effect of loop frequency on the peak intensity of the tilt-corrected images, we observed HIP57632 with different frame rates. The frame rate was changed by adjusting the exposure time of the sensing camera from 3 to 20 ms, yielding loop frequencies of 290 to 47 Hz.

In Figure 12, cross sections of the psfs with different loop frequencies are plotted. The peak intensity of the psf was increased with increase in loop frequency and the result is plotted in Figure 13. In this figure, the peak factor was defined as the ratio of peak intensity of the tilt corrected image to that of the uncorrected image.

Table 3 List of Observed Stars with Varying Angular Separation

Sl.No.	Target	RA	Dec	m_v	Δm_v	Sep ($''$)	LF (fps)	Peak factor	R (%)
1	HIP57632,–	11 49 03.5	+14 34 19.4	2.13	–	–	290	2.8,–	57,–
2	HIP54879,–	11 14 14.4	+15 25 46.4	3.35	–	–	290	2.1,–	45,–
3	HIP37279,–	07 39 18.1	+05 13 29.9	0.37	–	–	290	1.8,–	44,–
4	HIP65474,–	13 25 11.5	–11 09 40.7	0.97	–	–	290	1.4,–	32,–
5	HIP67927,–	13 54 41.0	+18 23 51.7	2.68	–	–	290	1.5,–	38,–
6	HIP69673,–	14 15 39.6	+19 10 56.6	–0.05	–	–	290	2.4,–	50,–
7	HIP50583, gam02 Leo	10 19 58	19 50 29.3	2.37	1.1	4.63	290	2.5, 2.1	52, 46
8	HIP61941, gam Vir B	12 41 39.6	–01 26 57.7	2.74	0.75	1.52	290	2.4, 2.3	51, 49
9	HR4677, HD 106976	12 18 08	–03 57 05.01	5.99	0.7	20.33	64	1.5, 1.3	36, 32
10	HR6752, 70 Oph B	18 05 27	02 30 0.0	4.03	2.04	4.91	98	1.9, 1.7	41, 36
11	HR5789, del Ser B	15 34 48.1	10 32 15.9	3.79	1.4	4.1	98	1.7, 1.5	32, 33
12	HR5984, bet02 Sco	16 05 26.2	–19 48 19.6	2.5	2.3	13.64	98	1.8, 1.6	42, 36
13	HR5505, eps Boo B	14 44 59.2	+27 04 27.2	2.39	2.4	2.58	98	1.8, 1.5	43, 31

m_v is apparent magnitude, Δm_v is magnitude difference between two objects and 'Sep' is angular separation between the objects in arcsec. Peak factor is the ratio of tilt corrected and uncorrected images, and improvement in resolution (R) is similar to Eq. (9). LF is approximate loop frequency.

We have modeled the effect of loop frequency on peak factor with a function in the form written in Equation (11)

$$I_{\rm pf}(f) = K_1 + K_2 * (1 - e^{-f_0/f}) \,. \qquad (11)$$

In the above equation, f is loop frequency, $I_{\rm pf}$ is peak factor and the estimated constants are K_1, K_2 and f_0, which are estimated to be ≈ 3.2, -2.2 and 52 Hz, respectively. The units of K_2 and K_1 are similar to that of $I_{\max}$. Arguably, the estimated values of the constants depend on the target intensity and the atmospheric seeing conditions.

In Figure 14, the power spectral densities for different loop frequencies are plotted. We can see that the correction bandwidth increased to $\sim$26 Hz at 290 Hz from $\sim$4.8 Hz at 47 Hz loop frequency. On average, the correction bandwidth is $\sim$1/10 of the loop frequency, which is in agreement with other studies reported in literature (Hardy 1998).

4.4 Gain in Angular Resolution

The tilt corrected images show improvement in angular resolution. The gain in angular resolution is a function of relative sizes of the telescope aperture (D) and the atmospheric coherence diameter r_0. This relation can be theoretically estimated by applying the formalism of Roddier (1981) and is displayed in Figure 15. The gain is defined as the ratio of equivalent width (Roddier 1981) of tilt uncorrected image and corrected images. The observed values of the gain for a set of six targets as listed in Table 3 are over plotted on the theoretical curve. r_0 is estimated from the equivalent width of the uncorrected images (to get D/r_0 for the observed data). The observed gain exhibits a deviation up to 24% from the theoretical gain.

4.5 Performance of the Instrument on Faint Targets

We observed a set of seven objects as listed in Table 3 (objects $7-13$) to validate the increase in sensitivity of the instrument due to image stabilization. Usually, a bright star near a faint star is used for sensing the image motions and the same correction is applied to the entire field. If the faint star is close enough, the corrections are similar and thus the sensitivity of the instrument on the faint star increases.

In Figure 16, the tilt uncorrected and corrected images of HIP50583 are displayed. The object has brightness of 2.37 in magnitude with a relatively fainter object with magnitude of 3.47, at an angular separation of 4.63$''$. The correction increased the peak intensity by a factor of $\sim$2.5 times for the brighter object and $\sim$2.1 times for the fainter object. The angular resolution (FWHM) of these objects improved by 52% and 46% respectively. Similar to this, several other objects were observed and these results are shown in Figure 17 and Table 3.

5 SUMMARY AND CONCLUSIONS

A tip-tilt instrument has been developed for the 1.3 m JCB telescope to overcome the image degradation caused by angle of arrival fluctuations. In laboratory, a simulated image motion corresponding to the actual data acquired from the telescope was used to characterize the instrument. The on-sky performance of the instrument was analyzed by observing several stars of varying brightness and angular separation. The real-time correction has manifested a characteristic improvement in the image quality that is consistent with previously reported studies in the literature. This study has led to the following findings and conclusions:

1. In the laboratory, the rms image motion was reduced by $\sim$12 times and the correction bandwidth was estimated to be $\sim$ 25 Hz for a loop frequency of 290 Hz.
2. At the telescope, the rms image motion was reduced by $\sim$14 times and the correction bandwidth was estimated to be about 0.1 times the loop frequency, where the loop frequency was varied from 47 Hz to 290 Hz (five distinct frequencies in this range).

3. The FWHM of the image reduced from 2.4″ to 1.03″. This corresponds to a 57% improvement in image resolution.
4. The sensitivity of the instrument was found to increase by a factor of 1.1 magnitude (corresponding to the increase in dynamic range, peak intensity ratio of 2.8).
5. In the case of targets with two close-by stars in the field, the FWHM of the individual psf decreased and the peak brightness increased depending on the magnitudes. For example, in the case of HIP50583 with separation of 4.63″ and magnitude difference of 1.1, the FWHM of the bright star increased by 52% and that of the faint star increased by 46%. The peak brightness of the bright star increased by a factor of $\sim$ 2.5 and that of the faint star increased by a factor of $\sim$ 2.1.

To further improve the image quality to that near the diffraction limited resolution of the telescope, work on a higher order AO system is in progress.

Acknowledgements We would like to thank Prof. B Raghavendra Prasad for allowing us to use the lab facilities at CREST. We also gratefully acknowledge the help received from Mr. Suresh Venkata Narra during the initial testing and from Mr. Hari Mohan Varsey for preparing the mechanical design of the instrument. We thank Mr. Anbazhagan, the engineer-in-charge, VBO Kavalur, for providing logistics and technical support during the on-sky testing. We also thank the observing staff at VBO, namely V. Moorthy, G. Selva Kumar, S Venkatesh, Rahul and Naveen for their valuable support during this work.

References

Close, L., & McCarthy, D. 1994, Publications of the Astronomical Society of the Pacific, 106, 77
Dainty, J. C., Koryabin, A. V., & Kudryashov, A. V. 1998, Applied optics, 37, 4663
Davis, J., & Tango, W. 1996, PASP, 108, 456
Eaton, F., Peterson, W., Hines, J., & Fernandez, G. 1985, Applied optics, 24, 3264
Fried, D. L. 1965, J. Opt. Soc. Am. A, 55, 1427
Fried, D. L. 1966a, J. Opt. Soc. Am. A, 56, 1372
Fried, D. L. 1966b, J. Opt. Soc. Am. A, 56, 1372
Glindemann, A. 1997, Publications of the Astronomical Society of the Pacific, 109, 682
Glindemann, A., McCaughrean, M. J., Hippler, S., et al. 1997, Publications of the Astronomical Society of the Pacific, 109, 688
Golimowski, D., Clampin, M., Durrance, S., & Barkhouser, R. 1992, Applied Optics, 31, 4405
Greenwood, D. P. 1977, JOSA, 67, 390
Hardy, J. W. 1998, Adaptive Optics for Astronomical Telescopes (Oxford Univ. Press), 448
Hubbard, G., Hege, K., Reed, M., et al. 1979, The Astronomical Journal, 84, 1437
Kellerer, A., & Tokovinin, A. 2007, A&A, 461, 775
Martin, H. M. 1987, PASP, 99, 1360
Max, C. E., Olivier, S. S., Friedman, H. W., et al. 1997, Science, 277, 1649
Noll, R. J. 1976, JOSA, 66, 207
Racine, R., & McClure, R. D. 1989, Publications of the Astronomical Society of the Pacific, 101, 731
Roddier, F. 1981, in Progress in Optics, 19 (Elsevier), 281
Rousset, G., Fontanella, J., Kern, P., Gigan, P., & Rigaut, F. 1990, Astronomy and Astrophysics, 230, L29
Russell, C. T. 1971, Cosmic Electrodynamics, 2, 184
Sarazin, M., & Tokovinin, A. 2002, in European Southern Observatory Conference and Workshop Proceedings, 58, 321
Sreekanth, R. V., Banyal, R. K., Sridharan, R., & Selvaraj, A. 2019, Research in Astronomy and Astrophysics, 19, 074
Welch, P. 1967, IEEE Transactions on Audio and Electroacoustics, 15, 70
Wizinowich, P. L., Acton, D. S., Lai, O., et al. 2000, Proc. SPIE 4007, Adaptive Optical Systems Technology